

# Preparation of hydrosol suspensions of elemental and core–shell nanoparticles by co-deposition with water vapour from the gas-phase in ultra-high vacuum conditions

Chris Binns · Pilar Prieto · Stephen Baker · Paul Howes · Ruggero Dondi ·  
Glenn Burley · Leonardo Lari · Roland Kröger · Andrew Pratt · Sitki Aktas ·  
John K. Mellon

Received: 7 March 2012 / Accepted: 13 August 2012  
© Springer Science+Business Media B.V. 2012

**Abstract** We report a new method to produce liquid suspensions of nanoparticles by co-deposition with water vapour from the gas-phase in ultra-high vacuum (UHV) conditions. The water is injected from outside the vacuum as a molecular beam onto a substrate maintained at 77 K and forms an ice layer with a UHV vapour pressure. Molecular dynamics simulations confirm that the nanoparticles are soft-landed close to the surface of the growing ice layer. We show that the un-agglomerated size distribution within the liquid is similar to the gas-phase size distribution and demonstrate that the inclusion of surfactants in the injected water prevents agglomeration. The method

allows the flexibility and tight size control available with gas-phase production methods to be applied to making nanoparticle suspensions with any desired properties. This is important for practical applications, especially in medicine. We have extended the method to include core–shell nanoparticles, in which there is flexible control over the core size and shell thickness and free choice of the material in either. Here, we report the production of suspensions of Cu, Ag and Au elemental nanoparticles and Fe@Au and Fe@Fe-oxide core–shell nanoparticles with diameters in the range 5–15 nm. We demonstrate the power of the method in practical applications in the case of Fe@Fe-oxide nanoparticles, which have a specific absorption rate of an applied oscillating magnetic field that is significantly higher than available Fe-oxide

This article is part of the topical collection on nanomaterials in energy, health and environment

C. Binns (✉) · S. Baker · P. Howes · S. Aktas  
Department of Physics and Astronomy, University  
of Leicester, Leicester LE1 7RH, UK  
e-mail: cb12@leicester.ac.uk

P. Prieto  
Departamento de Física Aplicada C-XII, Universidad  
Autónoma de Madrid, Cantoblanco, 28049 Madrid, Spain

R. Dondi  
Department of Chemistry, University of Leicester,  
Leicester LE1 7RH, UK

G. Burley  
Department of Pure and Applied Chemistry, University  
of Strathclyde, Glasgow G1 1XL, UK

L. Lari · R. Kröger · A. Pratt  
Department of Physics, University of York, Heslington,  
York YO10 5DD, UK

L. Lari  
The York JEOL Nanocentre, York Science Park,  
Heslington, York YO10 5BR, UK

J. K. Mellon  
Department of Cancer Studies and Molecular Medicine,  
University of Leicester, Leicester LE1 7RH, UK

nanoparticle suspensions and the highest yet reported. These will thus have a very high-performance in the treatment of tumours by magnetic nanoparticle hyperthermia.

**Keywords** Magnetic nanoparticle hyperthermia · Gas phase synthesis · Core-shell nanoparticles

## Introduction

Nanoparticles with diameters in the range 1–100 nm have become important entities in biological and medical research with a diverse variety of applications ranging from in vitro biomarkers to complex in vivo theranostic nanovectors that can both detect and treat disease (Rosi and Mirkin 2005; Haun et al. 2010; Solokov et al. 2003; Binns 2010). To perform in living tissue a nanoparticle needs to comprise several layers. Typically, there is a solid core a few nanometres across that is magnetic or optically active, coated with a layer that produces a stable suspension of the nanoparticle hydrosol and, for more advanced applications, further shells provide biological targeting and protection from the immune system. Ideally, to maximise performance for a given application, there needs to be complete flexibility of design of the nanoparticle core in terms of its constituent material, size and the ability to produce alloy and core-shell structures in which there is control over the core size and shell thickness. In addition, for medical applications, the final nanoparticles with their designed structure should be dispersed as a stable hydrosol in a fluid, preferably water.

Nanoparticles that are monodisperse (or at least have a narrow size distribution) are produced by a large number of techniques but the synthesis can be delineated into four basic classes, that is, chemical (Hyeon 2003; Sun et al. 2000; Boatman et al. 2005; Garcia-Martinez et al. 2003; Tsang 2008), biological (Coker et al. 2009; Narayanan and Sakthivel 2010), physical (Zhang et al. 2010a, b) and gas-phase (Binns 2001; Granqvist et al. 2005; Bouwen et al. 2000; Perez et al. 2010; Getzlaff et al. 2004; Baker et al. 2010). The advantage of chemical methods which include sol-gel and dendrimer template synthesis is that they can cheaply generate relatively large amounts of nanomaterial with good size control that is already in the form of a hydrosol. Biological methods use natural processes in bacteria to grow nanoparticles and also have the

advantage that the nanoparticle synthesis is cheap and in the form of a hydrosol but it is difficult to obtain control of size over a wide range. They do, however, have the additional advantage that the nanoparticles are naturally biocompatible. Physical methods such as ball milling generate large amounts of nanomaterial but in the form of a powder that must then be made soluble by attaching ligands. Gas-phase methods include synthesis at atmospheric pressure such as flame, plasma and spark sources, which all produce large quantities of powders or high vacuum methods, which generate a beam of nanoparticles in vacuum.

The high vacuum gas-phase methods produce relatively small quantities of nanoparticles in vacuum, which is very far removed from a hydrosol environment so at first, sight it would not appear as a natural choice for the synthesis of nanomaterials in medicine. They do, however, have enormous advantages including very tight size control over a wide range (1–20 nm), the ability to form core-shell structures in which there is free choice of core and shell materials and independent control over the core size and shell thickness (Baker et al. 2010). It is also straightforward to use alloys in either the core (Bouwen et al. 2000) or the shell and it is even possible to modify the internal atomic structure of the nanoparticles (Baker et al. 2012). An important feature of a vacuum gas-phase nanoparticle source is that it can operate in ultra-high vacuum (UHV) conditions (Baker et al. 2000; Iles et al. 2009) so that both the core and the shell can be reactive materials and remain pristine without being converted to oxide. With this level of control, the flexibility of design criterion is met, and more importantly, it is possible to ‘design’ the ideal nanoparticle by modelling and then manufacture it using the required materials with the pre-determined size and structure. The main technical problem is forming a hydrosol out of the nanoparticles in the beam since the vast majority of liquids have a vapour pressure that is incompatible with UHV operation.

Here, we report a simple solution to this problem and demonstrate the deposition of gas-phase nanoparticles into water by a method that preserves the UHV environment in the source region where the clusters are formed by maintaining the water temperature at 77 K. The method is flexible and will work with any liquid whose vapour pressure is sufficiently low at 77 K or above. Further, we describe how we coat the gas-phase nanoparticles with thin layers of other metals, prior to their deposition into water to form hydrosols of

core-shell particles. We will also report on methods to passivate the nanoparticles within the hydrosol to prevent agglomeration and form stable long-lived suspensions of isolated particles. With these issues addressed, it is now possible to produce hydrosols whose nanoparticles can be designed with the enormous flexibility available with cluster beam synthesis.

Finally, we will demonstrate the power of the method in applications by the synthesis of Fe@Fe-oxide nanoparticles with an exceptionally high value of the specific absorption rate (SAR) of an applied RF magnetic field. These will be powerful active components in nanovectors for the treatment of tumours by Magnetic Nanoparticle Hyperthermia (MNH). This method has reached Phase 2 human clinical trials (Maier-Hauff et al. 2007) but currently, due to the relatively low SAR of the available maghemite ( $\text{Fe}_2\text{O}_3$ ) nanoparticles, it is unable to work on its own and is used in conjunction with chemo- or radiotherapy. It remains a goal to make it work as a stand-alone therapy in which case it would make a very low morbidity and generic treatment.

## Experimental methods and theoretical models

### Core nanoparticle production

Two cluster beam sources were used in this work. In one, the core nanoparticles are formed in a sputter gas aggregation source based on the NCU200 source built by Oxford Applied Research Ltd. The design follows closely the original nanoparticle sputter source originally reported by Haberland et al. (1992). The 50-mm diameter metal target is sputtered using Ar gas at a sufficiently high pressure ( $\sim 1$  mbar) for the metal vapour to be supersaturated and condense into nanoparticles. The peak of the log-normal size distribution occurs at a particle size that depends on the inert gas pressure and sputtering power used but typically, it is possible to vary the most probable size between 5 nm and 15 nm particle diameter. An ultra-high mass RF quadrupole filter described earlier (Baker et al. 1997) can further size-select and produce a distribution with a mass ( $M$ ) and spread ( $\Delta M$ ) with values of  $\Delta M/M \sim 5\%$ . For the nanoparticle suspensions recorded here, however, this filtering was not used because of the reduction in flux and instead the quadrupole was used only to record the mass spectrum of the gas-phase nanoparticles prior to deposition.

The other source used in the work was a thermal gas aggregation source described previously (Baker et al. 2000; Iles et al. 2009). With this machine, the metal vapour is produced by a high temperature crucible and is mixed with He, cooled by liquid nitrogen to produce supersaturation. The crucible can operate at temperatures up to 2000 K so that transition metal nanoparticle beams can be generated. In general, this source produces nanoparticles with diameters in the range 1–4 nm.

In both sources, prior to introducing the rare gas used to assist nanoparticle condensation, the vacuum in the deposition chamber is in the  $10^{-10}$  mbar region. During deposition, the partial pressure of contaminant gases (mainly CO) in the deposition chamber with differential pumping (without water injection—see below) can be maintained in the  $10^{-11}$  mbar region (Iles et al. 2009) so that UHV-clean conditions persist throughout the process of cluster formation and deposition enabling even reactive nanoparticles to be deposited without oxidation. The combination of the two sources enables virtually any solid element or alloy to be produced as a nanoparticle beam with a controlled size over a wide range.

### Water deposition

The method used to deposit the nanoparticles into water while maintaining UHV-clean conditions in the rest of the source is illustrated in Fig. 1. The water

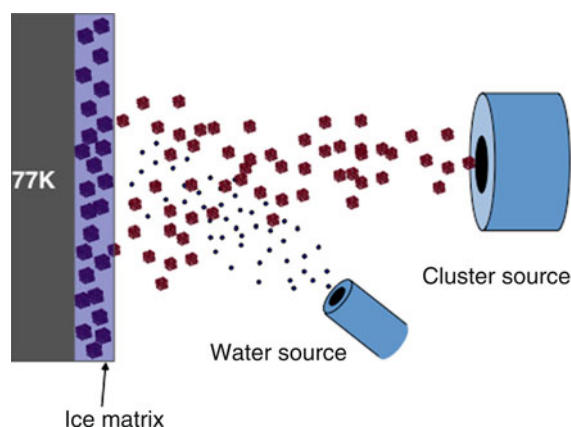


**Fig. 1** In order to achieve water deposition while maintaining UHV-clean conditions in the rest of the cluster source, the nanoparticles are deposited onto a substrate maintained at 77 K onto which impinges a molecular beam of water. The clusters are thus embedded into a growing ice layer and the volume fraction is determined by the relative deposition rates of nanoparticles and water. The vapour pressure of the ice at 77 K is in the range  $10^{-12}$  to  $10^{-14}$  mbar (Kouchi 1987)

vapour is introduced into vacuum as a molecular beam at a rate controlled by a Bronkhorst liquid flow controller and typically of the order of  $1 \text{ mL h}^{-1}$ . The beam impinges on a liquid nitrogen cooled surface while the nanoparticles are deposited onto the same surface and are embedded within the ice matrix. As shown by the molecular dynamics simulations presented below, the nanoparticles, which have typical speeds of around  $50 \text{ ms}^{-1}$ , are soft-landed and suffer no significant distortion as they are buried in the ice so they can be assumed to retain their equilibrium pseudo-spherical shape. The vapour pressure of crystalline ice is less than  $10^{-14} \text{ mbar}$  at  $77 \text{ K}$ ; however, the condensation method makes it more appropriate to use the value for amorphous ice, which can be two orders of magnitude higher (Kouchi 1987). This is still far too low to contaminate the gas-phase nanoparticles during their formation. This does, however, assume a sticking probability of 1 for the water molecules impinging on the cold substrate. When opening the water flow control valve, even with the substrate at  $77 \text{ K}$ , a rise in pressure to  $\sim 10^{-7} \text{ mbar}$  is observed due to the small fraction of water molecules reflected from the surface. Rapid pumping in the deposition chamber and the pressure differential along the nanoparticle source ensures that the cluster formation area, which is at a rare-gas pressure of  $\sim 1 \text{ mbar}$ , remains clean. The injected water was ultrapure and de-ionised with an electrical resistivity of  $18.2 \text{ M}\Omega$  and for some studies contained dissolved surfactants as described in ‘Results and discussion’ section.

The volume fraction of the nanoparticles in the hydrosol can be simply adjusted by varying the relative deposition rates of the particles and the water vapour. When the required amount of sample has been produced, the deposition chamber is isolated and vented to clean nitrogen while the ice is allowed to melt. The suspension is collected in a metal cup suspended beneath the conical substrate.

#### Measurement of the nanoparticle size distribution in the hydrosols

The size distributions of the hydrosols were measured either by dynamic light scattering (DLS) using a Malvern Instruments Zetasizer or by directly imaging the scattered light from each particle and analysing its Brownian motion using a Nanosight LM10 instrument. The former method has the advantage that it can

detect particle sizes down to  $0.6 \text{ nm}$  while the latter, although it is limited to metal particles larger than about  $10 \text{ nm}$ , enables the observer to discriminate which particles are analysed. This is an advantage in samples in which agglomeration has occurred since the agglomerates can be distinguished from the isolated particles, while for DLS, the agglomerates dominate the scattering and obscure the signal from the smaller particles.

#### Passivation and stabilisation of nanoparticle suspensions

For all elemental and core-shell nanoparticles produced as hydrosols, the particles quickly agglomerated in pure water. The process begins as soon as the ice is melted, and by the time the sample is removed, it is often possible to see the agglomerates by eye as tiny black specks. The agglomeration in pure water is confirmed by the measurements using DLS or Brownian motion as described in ‘Results and discussion’ section. We attempted to passivate the nanoparticles to form stable suspensions, by adding various surfactants to the injected water. The substances tested included citric acid, thiols, dithiols, *N,N*-dimethylethylenediamine and dimercapto-succinic acid.

#### Production of core-shell nanoparticles

The core nanoparticles formed by either of the cluster sources could be coated in UHV conditions in the gas phase by passing them through a heated tubular crucible containing the coating material as illustrated in Fig. 2a. The increase in mass of the particles due to the coating can be detected using the quadrupole mass filter as shown in Fig. 2b for Cu nanoparticles coated with Au. The open circles represent the mass spectrum for the core Cu particles recorded with the shell evaporator cold and the circles display the change in the mass spectrum with the Au shell evaporator heated to  $1472 \text{ K}$ . The uncoated core nanoparticles have a most probable mass of  $700,000 \text{ Daltons}$ , that is, contain about  $11,000 \text{ atoms}$  with a diameter, assuming the bulk density, of  $5.7 \text{ nm}$ . After passing through the heated shell evaporator, the mass has increased to  $825,000 \text{ Daltons}$ , which corresponds to about  $635 \text{ Au atoms}$ , or about a monolayer, though this is probably an underestimate as discussed below. In addition, in this particular case, the Au will probably alloy with the

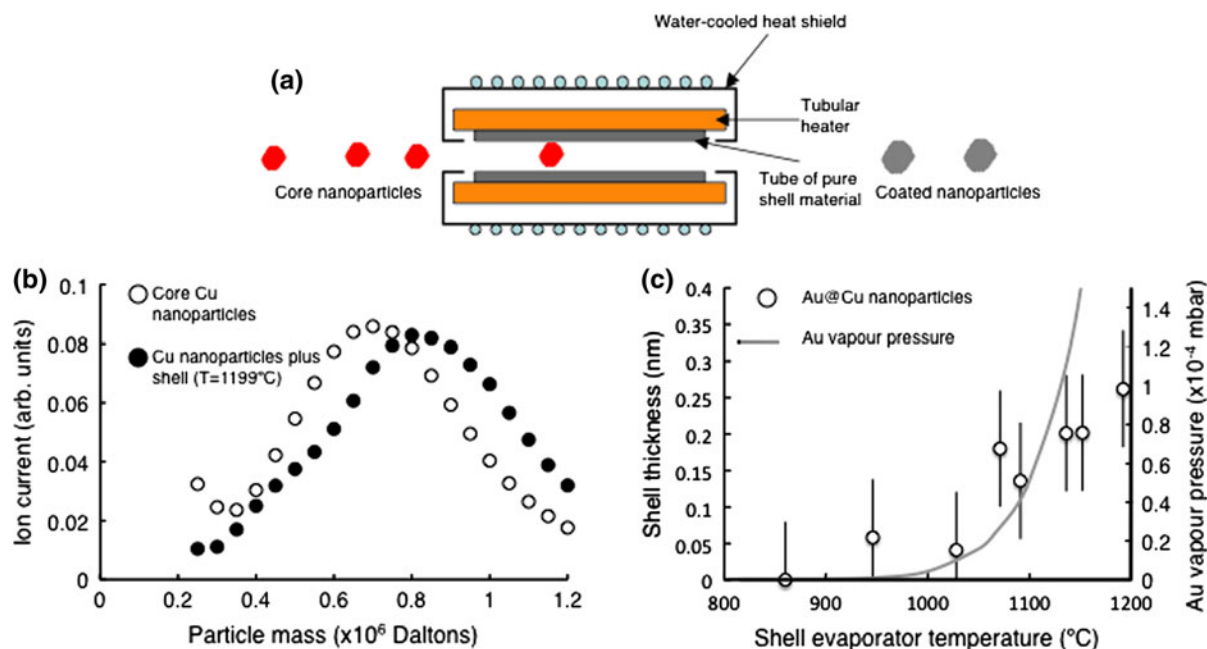


**Fig. 2** **a** Illustration of method used to coat the core nanoparticles with a shell in the gas phase. **b** Shift in measured mass of clusters with coating for Cu@Au nanoparticles. **c** Thickness of Au shell versus shell evaporator temperature (*open circles*)

compared to the vapour pressure of Au (*grey line*). The fall off in thickness at higher temperatures relative to the Au vapour pressure is ascribed to partial evaporation of the Cu core (see text)

core nanoparticle but the intention here was to demonstrate pick-up of the shell material.

The shell coating can be any material with a suitable vapour pressure to be evaporated in vacuum, and the shell thickness is controllable simply by changing the vapour pressure, that is, the temperature, within the shell evaporator. This is illustrated in Fig. 2c, which shows the increase in shell thickness as a function of evaporator temperature. Although the shell thickness does increase with temperature; it is clear that this does not follow the Au vapour pressure curve (grey line) and increases more slowly at higher temperature. We believe this is due to material evaporated from the Cu cores, which have a higher vapour pressure than Au, as the nanoparticles pass through the hot tube and this process will also accelerate the evaporation of Au off the surface. In general, therefore, the method works best if the vapour pressure of the core material, at the temperature of the shell evaporator, is significantly lower than the vapour pressure of the shell material. At all shell evaporator temperatures used, the direct evaporation of the shell material onto the substrate was insignificant.

### Structural determination

The atomic structure of Cu@Fe and Au@Fe nanoparticles was probed in EXAFS experiments carried out on beamlines I18 (Mosselmans et al. 2009) and BM29 (Filiponi et al. 2000) at the DIAMOND light source and European synchrotron radiation source (ESRF), respectively. Fe K edge, Cu K edge and Au L3 edge absorption spectra were measured in fluorescence using a nine-element monolithic Ge detector. After background subtracting and normalising the measured absorption spectra with the aid of the programme PySpline (Tenderholt et al. 2007), they were analysed to obtain structural information using the programme EXCURV98 (Binsted 1998). These experiments have recently been described in detail elsewhere (Baker et al. 2010).

Some particles were characterised by conventional (JEOL 2100) and aberration-corrected (JEOL 2200 FS) transmission electron microscopy (TEM) or scanning transmission electron microscopy (STEM). The samples were prepared either by directly depositing nanoparticles onto TEM grids in situ or by



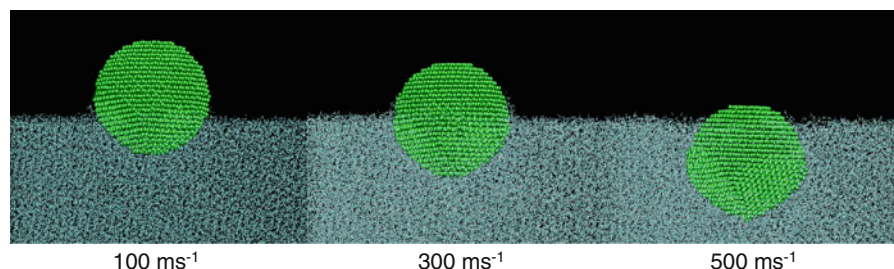


**Fig. 3** MD simulations of 5-nm diameter Au nanoparticles incident at the velocities shown coming to rest on the amorphous ice substrate. Even the fastest particles (which represent the

upper limit of possible velocities) show little damage and less than a particle diameter penetration into the substrate

preparing the liquid suspension and dripping a small amount of the suspension onto a holey carbon-coated copper grid followed by drying in air.

#### Measurement of SAR and modelling of heat production

The specific absorption rate of nanoparticle suspensions was measured by exposing them to oscillating magnetic fields with frequencies in the range 57 kHz to 263 kHz and measuring the change in temperature by focusing an infrared pyrometer onto the surface of the liquid. For all frequencies, the field amplitude was set so that the product of frequency times amplitude was at the Atkinson-Brezovich limit of  $4.85 \times 10^8 \text{ Am}^{-1} \text{ s}^{-1}$  (Atkinson et al. 1984; Pankhurst et al. 2009), which is often taken as the maximum safe limit for human exposure. The density of magnetic nanoparticles in our suspensions was kept low to minimise agglomeration and was typically  $0.06 \text{ mg mL}^{-1}$ .

#### Molecular dynamics of nanoparticle–ice interaction

In order to understand the details of vacuum deposition into amorphous ice and assess the level of particle damage and penetration into the ice, we performed molecular dynamics simulations of spherical gold nanoparticles with a diameter of 5 nm landing with different velocities on the ice substrate. The Au particles in our simulations were assigned velocities in the range  $50\text{--}500 \text{ ms}^{-1}$  in the direction normal to the ice surface, and the collision simulated using the LAMMPS software (Plimpton 1995).

The simulations used a rectangular box  $75 \times 75 \times 400 \text{ nm}^3$  with periodic boundary conditions imposed in each direction. The box contained a slab of

amorphous ice with a depth of 300 nm formed by simulating the rapid cooling of water from 300 to 90 K with a Nose–Hoover style barostat and thermostat. The bottom layers were fixed so that the ice slab did not recoil when struck by the gold particle. A spherical gold nanoparticle with an fcc lattice and a diameter of 5 nm was created above the ice surface. The atoms within the particle were assigned random velocities and positions to simulate a temperature of 300 K. During the simulation of the collision, the barostat and thermostat were removed.

The embedded atom potential (Foiles et al. 1986) was used to simulate Au–Au interatomic forces while the TIP4P (Jorgensen et al. 1983) model was used for the ice. The interaction between water molecules and the gold cluster was based on the Spohr model (Spohr 1998) of metal–water interaction potentials as modified by Dou et al. (2001) and Ju (2005) to take account of the non-planar geometry of spherical nanoparticles. Their potential is calculated by a pairwise summation with parameters chosen to match the experimentally derived adsorption energy for water. In this case, however, we are not interested in the detailed orientation of the first monolayer of water molecules so it was appropriate to simplify the model further. We therefore used a 12–6 Lennard-Jones potential between the oxygen and gold atoms whose parameters were chosen to reproduce the shape of Dou’s potential as closely as possible ( $\epsilon = 0.0668$ ,  $\sigma = 3.24$ ).

The velocity of the particles produced by the gas aggregation source is not precisely known but must be less than the velocity of the Ar atoms in a free jet expansion, which at room temperature corresponds to a mean Ar atom velocity of  $420 \text{ ms}^{-1}$ .

The results are illustrated in Fig. 3. They show that the penetration depth increases with nanoparticle velocity but even the fastest particles are not fully

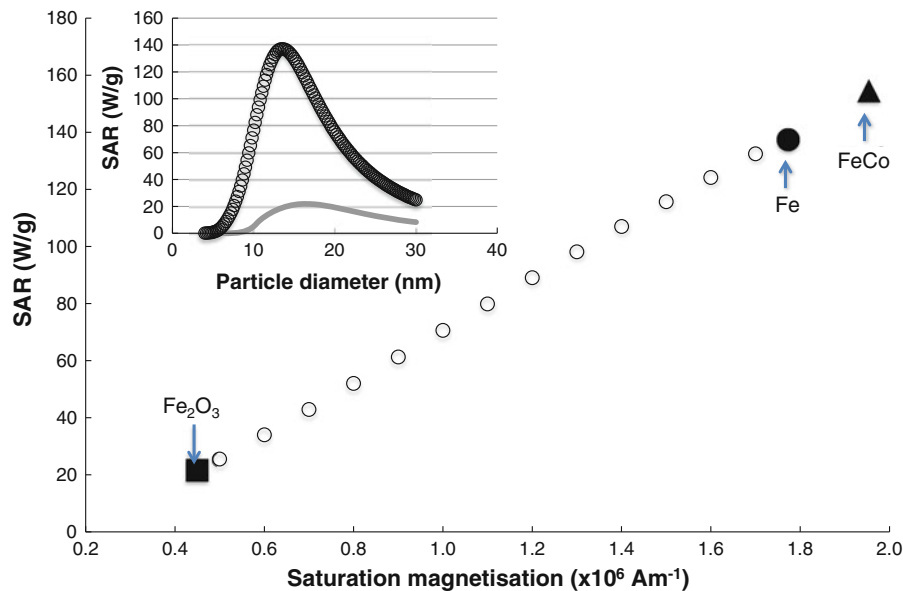


**Fig. 4** Dependence of SAR on the saturation magnetisation,  $M_S$ , of the material in the nanoparticles. The anisotropy constant,  $K$  and  $M_S$  for  $\text{Fe}_2\text{O}_3$  nanoparticles were taken from (Fiorani et al. 2002). The  $K$  value for Fe nanoparticles was taken from (Binns et al. 2002) and the bulk  $M_S$  was assumed. For FeCo, the  $K$  value for Fe nanoparticles and the bulk  $M_S$  value

embedded (4 nm depth for  $500 \text{ ms}^{-1}$  particles) and suffer only minimal distortion upon impact. We therefore conclude that nanoparticle agglomeration is unlikely during the deposition phase.

#### Calculation of the specific absorption rate of magnetic nanoparticles

In order to compare our measurements of the specific absorption rate (SAR) of the magnetic nanoparticles with theory, we have used the linear Néel-Brown relaxation model described by Rosensweig (2002). Although this has been superseded by models that include non-linear hysteretic heating effects (Hergt et al. 2008, 2010) it still provides a useful tool to analyse the experimental data. The model becomes invalid for large particles or large applied field amplitudes and generally provides an underestimate of the heating generated (Hergt et al. 2010).

The model is based on two heating mechanisms, that is, the Brownian mechanism due to the stochastic vibrations in the surrounding environment and the Néel mechanism due to the magnetisation vector rotating within the nanoparticle. The two mechanisms introduce time constants into the motion of nanoparticle

was used. For the  $M_S$  values between  $\text{Fe}_2\text{O}_3$  and pure Fe, the  $K$  value and material density were interpolated between the end points. The excitation field was 100 kHz at  $4,850 \text{ Am}^{-1}$ . The inset shows the particle size dependence of the SAR for  $\text{Fe}_2\text{O}_3$  nanoparticles (line) and Fe nanoparticles (open circles)

magnetisation vector labelled  $\tau_B$  and  $\tau_N$ , respectively. These are given by:

$$\tau_B = \frac{3\eta V_H}{kT},$$

where  $\eta$  is the medium viscosity and  $V_H$  is the hydrodynamic volume (magnetic core plus any shell) of the nanoparticle and

$$\tau_N = \frac{\sqrt{\pi}}{2} \tau_0 \frac{e^\Gamma}{\Gamma^{3/2}} \quad \text{with } \Gamma = \frac{KV_M}{kT}$$

where  $V_M$  is the volume of the magnetic core,  $K$  is the anisotropy constant of the magnetic material and  $\tau_0$  is the natural time constant of the magnetic moment (high temperature rotation limit).

If an oscillating magnetic field is applied to the nanoparticle, the time constants introduce a phase lag between the magnetic moment and the field, which pumps energy into the system as the vector rotates. The two time constants are combined to give a single time constant:

$$\frac{1}{\tau} = \frac{1}{\tau_B} + \frac{1}{\tau_N}$$

For an applied alternating magnetic field given by:

$$H(t) = H_0 \cos \omega t,$$

the imaginary (lossy) part of the complex susceptibility is given by:

$$\chi'' = \frac{\omega \tau}{1 + (\omega \tau)^2} \chi_0$$

where  $\chi_0$  is the temperature dependent susceptibility of the nanoparticle assembly and contains the volume fraction of magnetic material in the fluid. In general, for calculating the SAR values intrinsic to the material, the volume fraction is set to 1. For superparamagnetic nanoparticles,  $\chi_0$  is described by a Langevin function. The power generated is given by

$$P = \mu_0 \pi f H_0^2 \chi''$$

So in summary, the three main parameters of the nanoparticles that determine their SAR are their size (both hydrodynamic and magnetic volume), which determines the time constants  $\tau_B$  and  $\tau_N$ , the anisotropy constant,  $K$ , of the magnetic material, which determines  $\tau_N$  and the saturation magnetisation,  $M_S$ , of the magnetic material, which determines  $\chi_0$  at a given temperature. Figure 4 shows calculations of the peak value of SAR from a nanoparticle colloid as a function of  $M_S$ . The  $K$  and  $M_S$  values of  $\text{Fe}_2\text{O}_3$  (maghemite—the currently used material for MNH) and pure Fe nanoparticles are known and all the points in between have been calculated by interpolating the  $K$  and  $M_S$  values between those of maghemite and pure Fe. The inset in Fig. 4 shows the size dependence of SAR for maghemite and pure Fe. It is clear from Fig. 4 that to optimise SAR the key requirements are to have nanoparticles with a high saturation magnetisation and good size control, both of which are achieved with our synthesis method.

## Results and discussion

### Particle sizing and control of agglomeration

#### Silver nanoparticles

Figure 5a, b show the DLS results of two silver nanoparticle solutions in pure water with 0.03 and 0.4 mg mL<sup>-1</sup> concentration respectively where the agglomeration is clearly visible. We have also investigated the effect of ultrasonic excitation on the

stability of the suspensions and the results are included in Fig. 5. It can be observed that the ultrasonic excitation breaks up the aggregates, however, after a few hours, the nanoparticles start to aggregate again and tend to the original size distribution.

In order to stabilise the suspension, we introduced (9.1 mM) *N,N'*-dimethylethylenediamine:  $\text{C}_4\text{H}_{12}\text{N}_2$  (DMEDA) as a passivating agent into the water injected into the vacuum system and the DLS results are shown in Fig. 5c. A significant reduction of the hydrodynamic radii was observed in the as-deposited samples and after ultrasonic excitation with peaks in the DLS spectra at 11 and 7 nm. This results correlates with the presence of a yellow colour observed in the solution.

We observed that stable suspensions of small particles <10 nm in solution were coloured yellow and exhibited a single strong absorption due to the surface plasmon resonance (SPR) at ~400 nm as reported in previous work using conventionally synthesised Ag hydrosols (Evanoff and Chumanov 2005). Figure 6 shows the UV–Vis absorbance of silver nanoparticles in an aqueous DMEDA solution. The collected liquid ( $\text{Ag}_3$ ) was separated into two samples and one was not processed further while the other was treated by ultrasonic excitation for 1 h at 70 °C. A strong plasmon resonance at 405 nm is observed in both samples when measured as soon as possible after deposition (or deposition plus ultrasonic) as shown by the black points in Fig. 6a, b. Both figures show the change in the absorbance after being left for 3 days (red points). The untreated sample shows no plasmon resonance and also no yellow colour, which we ascribe to agglomeration, also indicated by the appearance of visible black specks in the water. The sample that was treated with ultrasonic excitation at 70 °C just after deposition remained yellow and as demonstrated by the red points in Fig. 6b, showed only a slight reduction of the SPR. We conclude that the further processing step is required to efficiently cover the nanoparticles with ligands after deposition.

We performed TEM measurements on this sample after 2 months (Fig. 6b inset) and the images indicate that the sample is mainly composed of nanoparticles smaller than 10 nm; however, it is possible to also find some aggregates that are the cause of a significant decrease of the plasmon signal in the UV–Vis spectrum as well the aggregation observed in DLS measurements after 2 months.



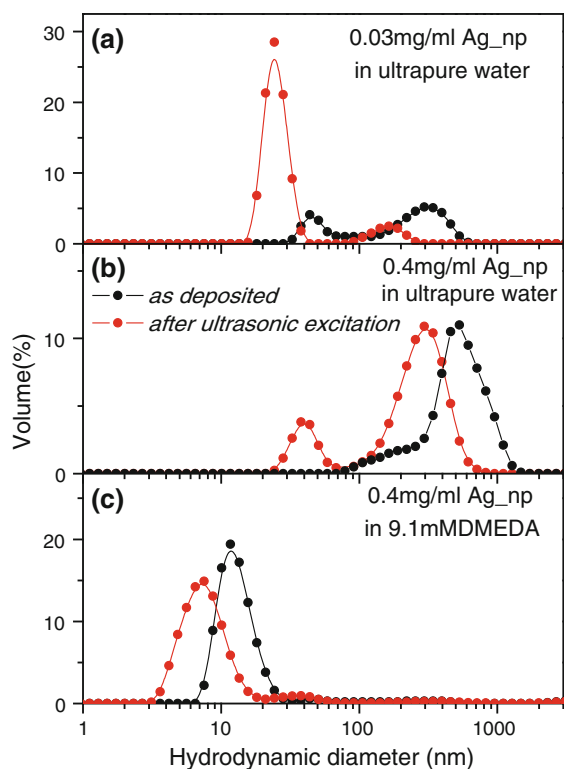


**Fig. 5** Average hydrodynamic diameter of silver nanoparticles as deposited and after ultrasonic excitation. **a** and **b** Silver nanoparticles in ultrapure water. **c** Silver nanoparticles in DMEDA

### Gold nanoparticles

In the case of suspensions of gold nanoparticles produced by the gas-phase deposition two surfactants, that is, mercapto-hexanol (Sigma-Aldrich 97 %) and dihydrolipoic acid, were tested to stabilise the

hydrosols. Both these exploit the strong gold-sulphur bond and are frequently used to stabilise gold nanoparticle suspensions. The best results were obtained with mercapto-hexanol in aqueous solution and a summary of the DLS results are shown in Fig. 7a, which compares the size distributions obtained when co-depositing the nanoparticles with pure water with those when the water contains the ligand, in both cases for the same nanoparticle concentration of  $0.3 \text{ mg mL}^{-1}$ . Including the ligand in the injected water maintains a significant fraction of the hydrosol at the deposited nanoparticle size whereas all particles are agglomerated when pure water is used. The results in Fig. 7b compares data from samples synthesised with three different nanoparticle concentrations, that is,  $0.02 \text{ mg mL}^{-1}$  (Au1),  $0.3 \text{ mg mL}^{-1}$  (Au2) and  $1.1 \text{ mg mL}^{-1}$  (Au3) but the same surfactant concentration and it can be observed that for the lowest concentration in 20 mM mercapto-hexanol solution the size spectrum is dominated by a single peak at 22 nm. Figure 7c shows the effect of changing the mercapto-hexanol concentration in the injected water for the same nanoparticle concentration, i.e.  $0.02 \text{ mg mL}^{-1}$ . We observe that increasing the ligand concentration from 20 to 200 mM decreases the stability of the suspension, which shows a large peak of agglomerates with a hydrodynamic diameter of 300 nm similar to that found in the as-deposited sample in pure water. It appears that too high a concentration of the mercapto-hexanol encourages agglomeration mediated by the ligands and the optimum concentration corresponds to around 20 mM. In summary, the Au hydrosol can be stabilised for a sufficiently low nanoparticle volume fraction and with the optimum ligand concentration.

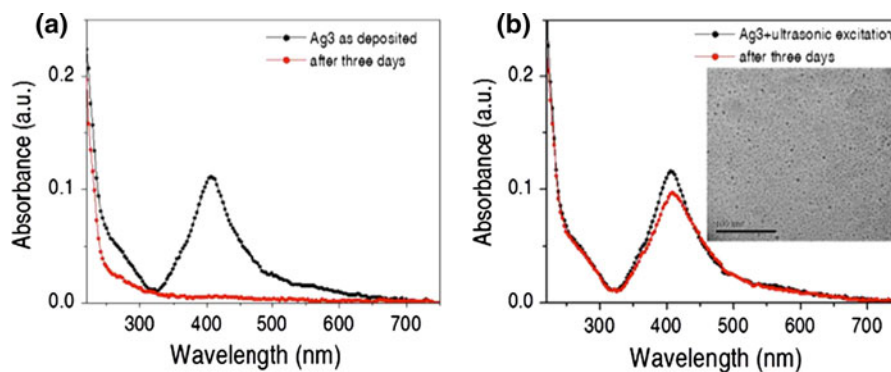


**Fig. 6** UV-Vis absorption spectra of silver nanoparticles in DMEDA solution measured as-deposited (**a**) and after 1 h ultrasonic excitation (**b**). The figures also included the spectra

after 3 days. *Inset* of (**b**) shows the corresponding TEM micrograph after 2 months indicating the presence regions without aggregates in the sample

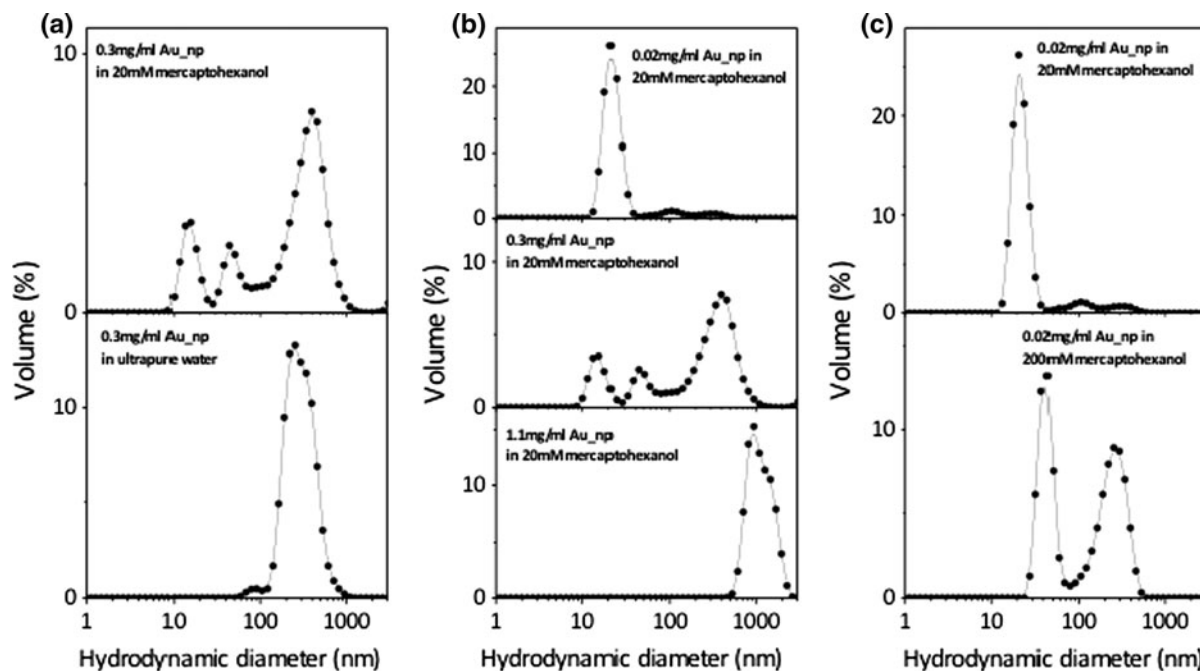


**Fig. 7** Average hydrodynamic diameter of different gold nanoparticle concentrations in different solutions. **a** Shows a comparison of the same gold nanoparticle concentration in ultrapure water and in a 20 mM mercapto-hexanol solution.

**b** Shows a comparison of different nanoparticle concentrations in the same surfactant solution and **c** shows a comparison between different surfactant concentration solutions for the same nanoparticle concentration

It was observed that the more concentrated solutions (Au2 and Au3), change colour quickly within the first 10 min from dark purple to black indicating that the aggregation starts immediately. We performed UV–Vis absorption measurements in the as-deposited samples (Fig. 8) where, even with a low intensity signal, it is possible to distinguish a wide plasmon resonance that shifts as a function of gold nanoparticle concentration in a fixed concentration 20 mM mercapto-hexanol solution. For the more concentrated sample, i.e. Au2 ( $1.1 \text{ mg mL}^{-1}$ ) the plasmon resonance appears at 650 nm but shifts to 580 nm for a concentration of  $0.3 \text{ mg mL}^{-1}$ . Finally for the lowest concentration, i.e.  $0.02 \text{ mg mL}^{-1}$ , two absorption bands appear at 450 and 350 nm. This wavelength shift seems to be related to a higher interparticle distance as the gold nanoparticle concentration decreases.

The optical properties of gold nanoparticles have been studied extensively and the effect on the absorption resonances of capping ligands, average interparticle separation and particle diameter are

known (Yang et al. 2007; Bellino et al. 2004; Köth et al. 2008). Plasmon resonance wavelengths at  $\sim 520 \text{ nm}$  have been reported in the literature for  $\leq 20 \text{ nm}$  gold nanoparticles, while higher wavelength absorbance bands are assigned to larger nanoparticle sizes and aggregates. For example, Yang et al. (2007) have found absorption bands at 585 and 630 nm related to linear-chain aggregates, while Bellino et al. (2004) have reported absorbance bands in the region 600–800 nm. These were attributed to gold nanoparticles capped with intermediate length thiols, similar to mercapto-hexanol, with the wavelength shift due to a decrease in the interparticle separation. In contrast, Köth et al. (2008) found absorption bands at shorter wavelengths  $\sim 420 \text{ nm}$  for smaller particles with diameters of about 2 nm.

Typical TEM images taken one month after deposition are shown in Fig. 8b where the presence of small nanoparticles  $< 5 \text{ nm}$  can be observed. This size is in good agreement with the nanocluster mass spectrum measured by mass RF quadrupole filter in vacuum before deposition into ice. The figure also shows how

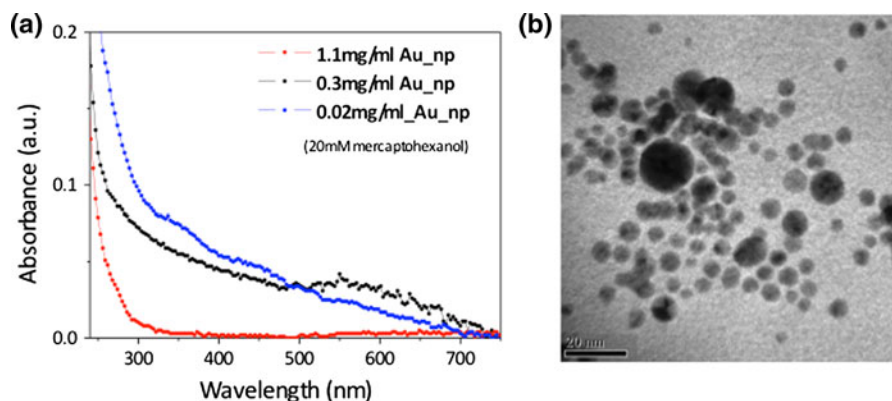


**Fig. 8** **a** UV–Vis absorption spectra of different concentrations of Au nanoparticles in 20 mM mercapto-hexanol solution. **b** TEM image of a sample with 0.3 mg mL<sup>-1</sup> Au nanoparticles in 20 mM mercapto-hexanol solution

the small nanoparticles aggregate in chains and round clusters. The shorter wavelength absorption bands observed for the lower concentration solution is also an indication of the presence of more isolated nanoparticles with smaller diameters. This kind of nanoparticle size distribution is not detected by DLS, whose signal is dominated by the larger particles and even small fractions of aggregates obscure the signal from the smaller particles.

### Iron nanoparticles

Iron nanoparticles have been deposited in both pure water and water with surfactant (dimercapto-succinic acid: C<sub>4</sub>H<sub>6</sub>O<sub>4</sub>S<sub>2</sub>) solutions by the described method at a concentration of 0.06 mg mL<sup>-1</sup>. DLS measurements in the as-deposited samples show agglomeration with mean diameters of ~1,000 nm. However, the Nano-sight LM10 instrument, in which the signal from the smaller particles is not obscured by the largest aggregates, shows a maximum at ~105 nm (Fig. 9a), which is still larger than the particles in the gas phase. In order to try and determine the composition of the hydrosol, we dried a drop of the suspension and obtained the aberration-corrected bright field STEM (BF-STEM) images shown in Fig. 10a, b. These reveal that the hydrosol comprises agglomerates of spherical and cubic particles with Fe cores around 10 nm, which is similar to the gas-phase mass spectrum. Figure 10b shows a high magnification BF-STEM image of a single Fe nanoparticle indicating the Fe@Fe-oxide core-shell structure with a 2.5 nm thick oxide shell and a 14 nm thick layer of surfactant.

For comparison, we also took some higher quality images of Fe nanoparticles deposited directly onto TEM grids in UHV and transferred through air into the microscope (Fig. 10c, d). The lower magnification image (Fig. 10c) again shows a mixture of cubes and spheres and the high-resolution image (Fig. 10d) reveals a similar thin oxide shell to the particles in suspension. In this case, it has been shown that the oxide proceeds via the well-known Cabrera-Mott process (Pratt et al. 2012) in which there is a self-limitation of the oxide film thickness. The first nanometre grows on a timescale of femtoseconds, the second on timescale of seconds, the third on a time scale of weeks and the fourth on a timescale of centuries.

The UV–Vis spectrum of iron nanoparticles in water solution are shown in Fig. 9b with an absorption at ~360 nm. Similar features in UV–Vis spectra have been observed in iron nanoparticles at 325 and 357 nm by Guo et al. (2001) and at 360 nm by Alqudami and Annapoorni (2007) and Zhang et al. (2010a, b). Guo et al. (2001) have also studied the evolution of these absorption peaks and found that their intensity decreases with the oxidation of Fe(0) nanoparticles. Because in this region no absorption of iron oxide nanoparticles has been observed previously, the absorption at 360 nm is an indication of an iron core-iron oxide shell structure in our samples in agreement with the TEM data.

### Heating studies of Fe@Fe-oxide nanoparticles

An important application of magnetic colloids is the treatment of tumours using MNH but it is clear from

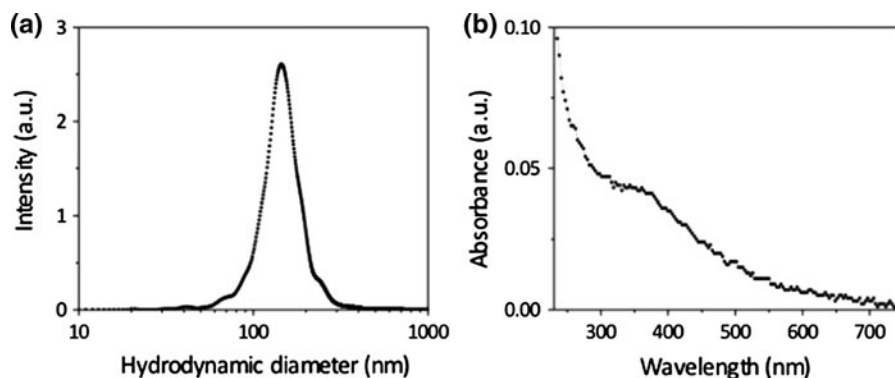


**Fig. 9** **a** Iron nanoparticle size distribution in water measured by the Nanosight LM10. **b** UV-Vis absorption spectra of iron nanoparticles in water/surfactant solution

Phase 1 human clinical trials (Johannsen et al. 2007) that there needs to be a significant improvement in the SAR of nanoparticle ferrofluids above that of the currently used maghemite suspensions. As discussed in ‘[Calculation of the specific absorption rate of magnetic nanoparticles](#)’ section the two most important factors are a high saturation magnetisation of the nanoparticles and good size control, which we have in the samples produced by our method.

Figure 11 shows the SAR measured from our Fe nanoparticles using the method described in ‘[Structural determination](#)’ section at four distinct frequencies of the applied field. At all frequencies the amplitude of the magnetic field was adjusted so that the product  $H \times f$  remained at the Atkinson-Brezovich limit of  $4.85 \times 10^8 \text{ Am}^{-1} \text{ s}^{-1}$  (Atkinson et al. 1984; Pankhurst et al. 2009) thus the SAR could be determined with an excitation field that is safe for clinical use. The solid line through the data is calculated using the linear Néel-Brown relaxation model described in ‘[Molecular dynamics of nanoparticle-ice interaction](#)’ section with no adjustable parameters. The median diameter of the nanoparticles (14 nm) and the shell thickness (2.5 nm) was obtained from the TEM images, the saturation magnetisation of the core was taken to be that of bulk Fe ( $1.77 \times 10^6 \text{ Am}^{-1}$ ) and the anisotropy constant was  $2 \times 10^5 \text{ Jm}^{-3}$  as previously measured from Fe nanoparticles (Binns et al. 2002). It was assumed in the calculation that the Fe-oxide shell is non-magnetic though it is possibly one of the ferrimagnetic oxides. The effect of this is likely to be small as the saturation magnetisation of maghemite or magnetite at ideal

stoichiometry is only about 25 % that of pure Fe. A secondary effect of a ferrimagnetic oxide could be a modification of the nanoparticle anisotropy due to the ferrimagnetic/ferromagnetic interface, which again is likely to be a relatively small effect. For comparison, the calculation for 14-nm diameter pure  $\text{Fe}_2\text{O}_3$  nanoparticles with no shell is shown by the dashed line.

The calculation agrees with the measurements at intermediate frequencies but underestimates the SAR at low frequency. This may well be due to the fact that the lowest frequency used (57 kHz) corresponded to the highest amplitude of the field ( $8.5 \times 10^3 \text{ Am}^{-1}$ ) and the heating mechanism could be entering the non-linear regime where it has been predicted by Hergt et al. (2010) that the SAR exceeds the values predicted by the linear model.

In the last few years, a number of new synthesis routes to produce new types of magnetic nanoparticle ferrofluids have been developed in an attempt to maximise their SAR. These include magnetite nanoparticles produced by magnetotactic bacteria (Hergt et al. 2005), Co@CoO core-shell nanoparticles prepared by thermolysis of  $\text{Co}_2(\text{CO})_8$  (Hergt et al. 2006; Bönnemann et al. 2003) and chemically synthesised Fe(0) nanocubes (Mehdaoui et al. 2010) all of which have higher SAR values than maghemite.

A problem in comparing nanoparticles used by different groups is that reports of SAR use different field excitation frequencies and amplitudes, often far above the Atkinson-Brezovich limit and it is not clear how to scale them to produce a comparison of the fundamental performance of the material. A scheme that has been suggested by Kallumadil et al. (2009) is



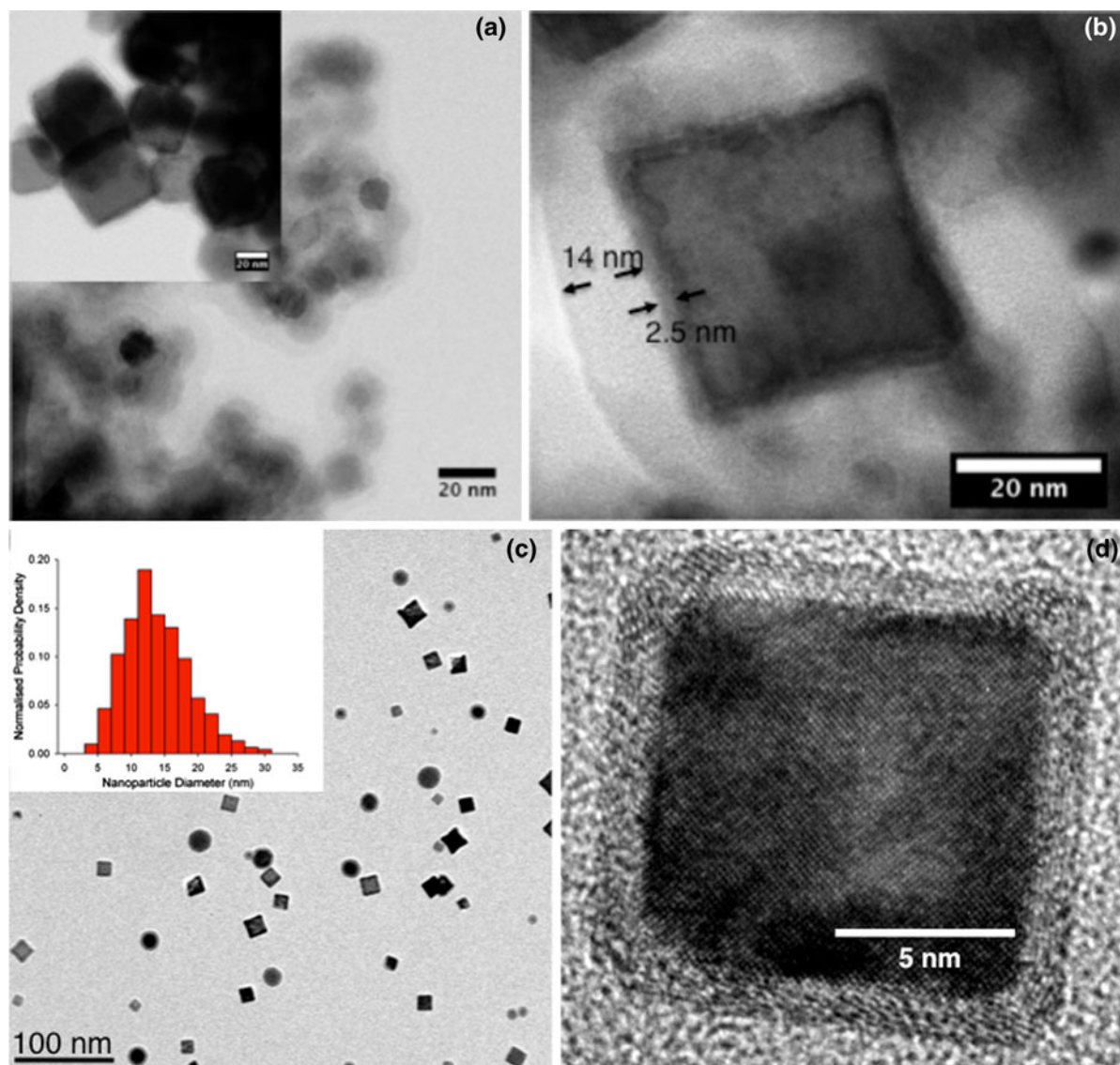


**Fig. 10** **a** and **b** BF-STEM images of Fe nanoparticles extracted from water with dimercapto-succinic acid and dried on a TEM grid with each showing a pure Fe core, a thin oxide shell and a thicker surfactant shell. **c** and **d** BF-STEM images of

Fe nanoparticles deposited in vacuum directly onto TEM grids allowing higher resolution. The same core-shell Fe@Fe-oxide structure is observed and a lattice spacing corresponding to bulk bcc Fe is visible in the core

to convert the measured SAR to an intrinsic loss parameter (ILP) defined by:

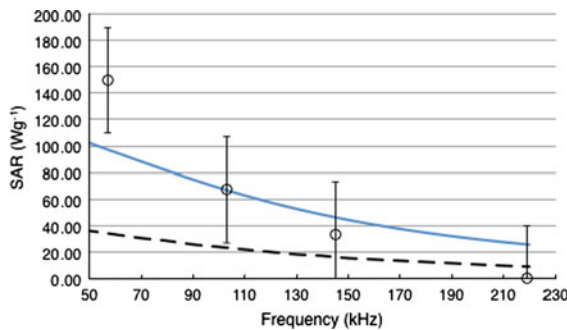
$$ILP = \frac{SAR}{H^2 f}$$

where  $H$  and  $f$  are the amplitude and frequency of the excitation field respectively. This normalises out the  $H^2 f$  dependence of SAR predicted by the linear relaxation model and should depend only on the performance of the material. This is a helpful tool and

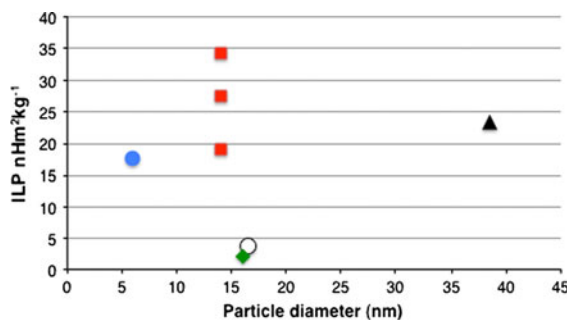
has been used to compare the performance of a number of commercial magnetic colloids for hyperthermia (Kallumadil et al. 2009). We also use the ILP in our comparisons of different materials below but it should be remembered that this is only valid within the validity limits of the linear relaxation model (small particles and low field amplitudes).

Figure 12 shows the ILP (which has units  $\text{Wsm}^2 \text{kg}^{-1} \text{A}^{-2}$  or  $\text{Hm}^2 \text{kg}^{-1}$ ) measured for maghemite as well as the higher performance materials listed





**Fig. 11** Measured SAR values from 14-nm diameter Fe@Fe-oxide core-shell nanoparticles produced by the new method at four discrete frequencies of the applied magnetic field. At each frequency, the amplitude of the field was adjusted so that the product  $H \times f$  was at the Atkinson-Brezovich limit of  $4.85 \times 10^8 \text{ Am}^{-1} \text{ s}^{-1}$  (Atkinson et al. 1984; Pankhurst et al. 2009). The solid line shows a calculation using the linear Néel-Brown relaxation model with no adjustable parameters (see text for all the values used). On comparison, the dashed line shows the same calculation for 14-nm diameter  $\text{Fe}_2\text{O}_3$  nanoparticles



**Fig. 12** ILP measured for various high-performance ferrofluids containing different-sized nanoparticles developed for hyperthermia. Filled circle: Co@Co oxide nanoparticles synthesised by Bönnemann et al. (2003) and measured by Hergt et al. (2006). Filled triangle: magnetite nanoparticles produced by magnetotactic bacteria measured by Hergt et al. (2005). Filled diamond: Fe(0) nanocubes synthesised by Mehdaoui et al. (2010). Open circle: Maghemite nanoparticles synthesised by Fortin et al. (2007). Filled squares: Fe@Fe-oxide nanoparticles described here measured at three different frequencies

above. The value measured for maghemite nanoparticles is represented by the open circle and marks the performance of material currently used for MNH. The Co@CoO nanoparticles (filled circle) synthesised by Bönnemann et al. (2003) and measured by Hergt et al. (2006) and the magnetite nanoparticles produced by magnetotactic bacteria measured by Hergt et al. (2005) show much higher values of ILP. Surprisingly, the Fe(0) nanocubes synthesised by Mehdaoui et al. (2010), which appear quite similar to the particles

produced in this work, display a low value of ILP. Although a high value of SAR was reported by Mehdaoui et al. (2010), this was measured with a excitation field with an  $H \times f$  value over 30 times the Atkinson-Brezovich limit, which illustrates the problem in comparing SAR values in different reports. On the other hand, this sample was measured using a higher amplitude field ( $5.2 \times 10^4 \text{ Am}^{-1}$ ) than any of the other samples and the  $H^2 f$  scaling to obtain the ILP, which may not be a valid parameter in this case, could be artificially depressing the value for this sample.

In any case, the highest performance among all the samples is displayed by the Fe@Fe-oxide nanoparticles produced in this work and measured with an excitation field at the Atkinson-Brezovich limit. The ILP value is shown for the three different frequencies used that showed a measurable SAR and the fact that it is changing with frequency shows that the heating is not entirely described by the linear relaxation model. This performance is obtained without any optimisation such as varying the particle size or trying to control the anisotropy by introducing antiferromagnetic shells, etc., so we are confident that even higher values can be obtained in future.

#### Structural studies of core-shell nanoparticles by EXAFS

For Fe@Cu nanoparticles, thin Cu shells of 1–2 monolayers in thickness epitaxially match the bcc Fe core. Thicker shells of approximately 20 monolayers of Cu have the expected fcc structure of bulk Cu, and drive the atomic structure of the Fe core from bcc to fcc. Thus, for this combination of materials (and several others), the synthesis method provides a way to change the crystal structure of the core nanoparticle. Using CuAu alloy shells, it has been shown that even the lattice constant of the core can be controlled making it possible to synthesise ‘stretched lattice’ fcc Fe nanoparticles with a saturation magnetisation of  $2.5 \mu_B/\text{atom}$  (Baker et al. 2012).

In Fe@Au nanoparticles, the structure in the Fe core remains bcc (as in bulk Fe) although there is some stretch in the Fe lattice in the limit of thick Au shells. While the structure of the Au shell is essentially fcc (as in bulk Au), there is considerable contraction in the nearest neighbour atomic distances for Au shells 1–2 monolayers thick. Analysis of the nearest neighbour numbers show no evidence for alloying between Au and Fe thus indicating a sharp interface. This is not

unexpected as the Fe–Au system has a peritectic-type phase diagram (Massalski et al. 1986) and neither an intermediate phase nor an intermetallic compound exist in the equilibrium state.

## Conclusions

We have described a new method for synthesizing hydrosols of nanoparticles in which the nanoparticles are manufactured and processed (e.g. coated with shells) in the gas-phase in UHV-clean conditions and then deposited into liquids. It allows the synthesis of any type of nanoparticle, including core–shell structures in which there is free choice of the materials in the core or the shells and independent control over the core size and shell thickness. Extra flexibility is afforded by the ability with certain combinations of materials to change the crystal structure of the materials and even to some extent control the lattice constant. In addition, any liquid whose vapour pressure is in the UHV range at 77 K can be used. No other synthesis method allows such flexibility in the design of nanoparticle suspensions and it should be possible to optimise the performance of hydrosols in a range of applications. We have demonstrated this in the case of Fe@Fe-oxide nanoparticles in water, which show the highest SAR of any reported ferrofluid in response to an applied AC magnetic field and would be very high-performance nanovectors for magnetic nanoparticle hyperthermia treatment of tumours.

## References

- Alqudami A, Annapoorni S (2007) Metallic silver and iron nanoparticles prepared by exploding wire technique. *Plasmonics* 2:5
- Atkinson WJ, Brezovich IA, Chakraborty DP (1984) Usable frequencies in hyperthermia with thermal seeds. *IEEE Trans Biomed Eng* 31:70
- Baker SH, Thornton SC, Keen AM, Preston TI, Norris C, Edmonds KW, Binns C (1997) The construction of a gas aggregation source for the preparation of mass-selected ultra-small metal particles. *Rev Sci Instr* 68:1853
- Baker SH, Thornton SC, Edmonds KW, Maher MJ, Norris C, Binns C (2000) Characterisation of a gas aggregation source for the preparation of size-selected nanoscale transition metal clusters. *Rev Sci Instr* 71:3178
- Baker SH, Roy M, Qureshi M, Binns C (2010) Probing atomic structure in magnetic core/shell nanoparticles using synchrotron radiation. *J Phys Condens Matter* 22:385301
- Baker SH, Roy M, Thornton SC, Binns C (2012) Realizing high magnetic moments in fcc Fe nanoparticles through atomic structure stretch. *J Phys Condens Matter* 24:176001
- Bellino MG, Calco EJ, Gordillo G (2004) Adsorption kinetics of charged thiols on gold nanoparticles. *Phys Chem Chem Phys* 6:424
- Binns C (2001) Nanoclusters deposited on surfaces. *Surf Sci Rep* 44:1
- Binns C (2010) Introduction to nanoscience and nanotechnology, Chapter 6. Wiley, Hoboken
- Binns C, Maher MJ, Pankhurst QA, Kechrakos D, Trohidou KN (2002) Magnetic behaviour of nanostructured films assembled from preformed Fe clusters embedded in Ag. *Phys Rev B* 66:184413
- Binsted N (1998) EXCURV98: Daresbury Laboratory computer program
- Boatman EM, Lisensky GC, Nordell KJ (2005) A safer, easier, faster synthesis for CdSe quantum dot nanocrystals. *J Chem Educ* 82:1697
- Bönnemann H, Brijoux W, Brinkmann R, Matoussevitch N, Waldöfner N, Palina N, Modrow H (2003) A size-selective synthesis of air stable colloidal magnetic cobalt nanoparticles. *Inorg Chim Acta* 350:617
- Bouwen W, Thoen P, Vanhoutte F, Bouckaert S, Despa F, Weidele H, Silverans RE, Lievens P (2000) Production of bimetallic clusters by a dual-target dual-laser vaporization source. *Rev Sci Instrum* 71:54
- Coker VS, Telling ND, Van Der Laan G, Patrick RAD, Pearce CI, Arenholz E, Tuna F, Winpenny REP, Lloyd JR (2009) Harnessing the extracellular bacterial production of nano-scale cobalt ferrite with exploitable magnetic properties. *Proc Natl Acad Sci USA* 3:1922
- Dou Y, Zhigilei LV, Winograd N, Garrison BJ (2001) Explosive boiling of water films adjacent to heated surfaces: a microscopic description. *J Phys Chem A* 105:2748
- Evanoff DD, Chumanov G (2005) Synthesis and optical properties of silver nanoparticles and arrays. *Chem Phys Chem* 6:1221
- Filiponi A, Bocowski M, Bowron DT, Ansell S, De Panfilis S, Di Ciccio A, Itie J-P (2000) An experimental station for advanced research on condensed matter under extreme conditions at the European synchrotron radiation facility—BM29 beamline. *Rev Sci Instrum* 71:2422
- Fiorani D, Testa AM, Lucari F, D’Orazio F, Romero H (2002) Magnetic properties of maghemite nanoparticle systems: surface anisotropy and interparticle interaction effects. *Physica B* 320:122
- Foiles SM, Baskes MI, Daw MS (1986) Embedded-atom-method functions for the fcc metals Cu, Ag, Au, Ni, Pd, Pt, and their alloys. *Phys Rev B* 33:7983
- Fortin J-P, Wilhelm C, Servais J, Ménager C, Bacri J-C, Gazeau F (2007) Size-sorted anionic iron oxide nanomagnets as colloidal mediators for magnetic hyperthermia. *J Am Chem Soc* 129:2628
- Garcia-Martinez JC, Scott RWJ, Crooks RM (2003) Extraction of monodisperse palladium nanoparticles from dendrimer templates. *J Am Chem Soc* 125:11190
- Getzlaff M, Kleibert A, Methling R, Bansmann J, Meiwes-Broer K-H (2004) Mass-filtered ferromagnetic alloy clusters on surfaces. *Surf Sci* 566–568:332

- Granqvist C, Kish L, Marlow M (eds) (2005) Gas phase nanoparticle synthesis, Springer, Berlin. ISBN-13: 978-14020 24436
- Guo L, Huang Q, Li XY, Yang S (2001) Iron nanoparticles: Synthesis and applications in surface enhanced Raman scattering and electrocatalysis. *Phys Chem Chem Phys* 3:1661
- Haberland H, Karrais M, Mall M, Thurner Y (1992) Thin films from energetic cluster impact: a feasibility study. *J Vac Sci Technol A* 10:3266
- Haun JB, Yoon T-J, Lee H, Weissleder R (2010) Magnetic nanoparticle biosensors. *Nanomed and Nanobiotech* 2:291
- Hergt R, Hiegeist R, Zeisberger M, Schüler D, Heyen U, Hilger I, Kaiser WA (2005) Magnetic properties of bacterial magnetosomes as potential diagnostic and therapeutic tools. *J Magn Magn Mater* 293:80
- Hergt R, Dutz S, Müller R, Zeisberger M (2006) Magnetic particle hyperthermia: nanoparticle magnetism and materials development for cancer therapy. *J Phys Condens Matter* 18:S2919
- Hergt R, Dutz S, Röder M (2008) Effects of size distribution on hysteresis losses of magnetic nanoparticles for hyperthermia. *J Phys Condens Matter* 20:385214
- Hergt R, Dutz S, Zeisberger M (2010) Validity limits of the Néel relaxation model of magnetic nanoparticles for hyperthermia. *Nanotechnology* 21:015706
- Hyeon T (2003) Chemical synthesis of magnetic nanoparticles. *Chem Commun* 8:927
- Iles GN, Baker SH, Thornton SC, Binns C (2009) Enhanced capability in a gas aggregation source for magnetic nanoparticles. *J Appl Phys* 105:024306
- Johannsen M, Gneveckow U, Taymoorian M, Thiesen B, Waldoefner N, Scholz R, Jung K, Jordan A, Wust P, Loening S (2007) Morbidity and quality of life during thermotherapy using magnetic nanoparticles in locally recurrent prostate cancer: results of a prospective phase I trial. *Int J Hyperther* 23:315
- Jorgensen WL, Chandrasekhar J, Madura JD, Impey RW, Klein ML (1983) Comparison of simple potential functions for simulating liquid water. *J Chem Phys* 79:926
- Ju S-P (2005) A molecular dynamics simulation of the adsorption of water molecules surrounding an Au nanoparticle. *J Chem Phys* 122:094718
- Kallumadil M, Tada M, Nakagawa T, Abe M, Southern P, Pankhurst QA (2009) Suitability of commercial colloids for magnetic hyperthermia. *J Magn Magn Mater* 321:1509
- Köth A, Koetz J, Appelhans D, Voit B (2008) "Sweet" gold nanoparticles with oligosaccharide- modified poly(ethyl-eneimine). *Colloid Polym Sci* 286:1317
- Kouchi A (1987) Vapour pressure of amorphous ice and its astrophysical implications. *Nature* 330:550
- Maier-Hauff K, Rothe R, Scholz R, Gneveckow U, Wust P, Thiesen B, Feussner A, von Deimling A, Waldoefner N, Felix R, Jordan A (2007) Intracranial thermotherapy using magnetic nanoparticles combined with external beam radiotherapy: results of a feasibility study on patients with glioblastoma multiforme. *J Neurooncol* 81:53
- Massalski TB, Murray JL, Bennet LH, Baker H (eds) (1986) Binary alloy diagrams. American Society for Metals, Metals Park, p 368
- Mehdaoui B, Meffre A, Lacroix L-M, Carrey J, Lachaize S, Gougeon M, Respaud M, Chaudret B (2010) Large specific absorption rates in the magnetic hyperthermia properties of metallic iron nanocubes. *J Magn Magn Mater* 322:L49
- Mosselmans JFW, Quinn PD, Dent AJ, Cavill SA, Moreno SD, Peach A, Leicester PJ, Keylock SJ, Gregory SR, Atkinson KD, Rosell JR (2009) I18—the microfocus spectroscopy beamline at the diamond light source. *J Synchrotron Radiat* 16:818
- Narayanan KB, Sakthivel N (2010) Biological synthesis of metal nanoparticles by microbes. *Adv Colloid Interface Sci* 156:1
- Pankhurst QA, Thanh NKT, Jones SK, Dobson J (2009) Progress in applications of magnetic nanoparticles in biomedicine. *J Phys D* 42:224001
- Perez A, Melinon P, Dupuis V, Bardotti L, Masenelli B, Tournus F, Prevel B, Tuillon-Combes J, Bernstein E, Tamion A, Blanc N, Tainoff D, Boisson O, Guiraud G, Broyer M, Pellarin M, Del Fatti N, Vallee F, Cottancin E, Lerme J, Vialle J-L, Bonnet C, Maioli P, Crut A, Clavier C, Rousset JL, Morfin F (2010) Functional nanostructures from clusters. *Int J Nanotechnol* 7:523
- Plimpton SJ (1995) Fast parallel algorithms for short-range molecular dynamics. *J Comp Phys* 117:1
- Pratt A, Shah A, Lari L, Woffinden S, Tear SP, Binns C, Kröger R (2012) Initial-oxidation induced strain effects in Fe/Fe-oxide core-shell nanoparticles. *Nat Mater* (submitted)
- Rosensweig RE (2002) Heating magnetic fluid with alternating magnetic field. *J Magn Magn Mater* 252:370
- Rosi L, Mirkin CA (2005) Nanostructures in bionanotechnology. *Chem Rev* 105:1547
- Solovkov K, Follen A, Aaron J, Pavlova I, Malpica R, Lotan R, Richards-Kortum R (2003) Real-time vital optical imaging of precancer using anti-epidermal growth factor receptor antibodies conjugated to gold nanoparticles. *Cancer Res* 63:1999
- Spohr EJ (1998) Computer simulation of the structure of the electrochemical double layer. *J Electroanal Chem* 450:327
- Sun S, Murray CB, Weller D, Folks L, Moser A (2000) Monodisperse FePt nanoparticles and ferromagnetic nanocrystal superlattices. *Science* 287:1989
- Tenderholt A, Hedman B, Hodgson KO (2007) PySpine: a modern, cross-platform program for the processing of raw averaged XAS edge and EXAFS data. *13th Int Conf.XAFS: AIP Conf Proc* 882:105
- Tsang E (2008) Synthesis of clusters and nanoparticles by chemical methods in metallic nanoparticles. In: John Blackman (ed) *Handbook of metal physics*, vol 5. Elsevier, Amsterdam, chapter 4
- Yang Y, Matsubara S, Nogami M, Shi J (2007) Controlling the aggregation behavior of gold nanoparticles. *Mater Sci Eng B* 140:172
- Zhang G, Wei G, Zheng K, Li L, Xu D, Wang D, Xue Y, Su W (2010a) The synthesis of beta-SiC nanoparticles by high-energy mechanical ball milling and their photoluminescence properties. *J Nanosci Nanotechnol* 10:1951
- Zhang Y, Padhyay A, Sevilleja JE, Guarrant RI, Geddes CD (2010b) Interactions of fluorophores with iron-nanoparticles: metal-enhanced fluorescence. *J Phys Chem C* 114: 7575